Chapter 8

Multipartite entanglement for one photon among four optical modes

This chapter is largely based on ref.[35]. Reference[35] refers to the then current literature in 2009 at the time of publication.

8.1 Introduction

Investigations of entanglement for two quantum systems have answered many fundamental questions in quantum physics[219,273] and revealed powerful new capabilities of quantum mechanics within the field of quantum information science (refs.[1,3,162], see also chapter 1). Many of these advances have used well-tested methods for the characterization of quantum entanglement in bipartite (i.e., two-component) systems[40,110]. Entangled states of more than two systems enhance our knowledge of quantum theory, as new classes of states are available[40,209,210]. Beyond applications to conventional quantum computation[3], exotic multipartite states have emerged as crucial resources for new directions in quantum information processing such as measurement-based quantum computation[212,213], quantum secret sharing[274], and quantum simulation[5]. Despite the extraordinary promise that they offer, unambiguously detecting multipartite entangled states is still a major challenge from both an experimental and a theoretical standpoint.

Genuine N-partite entanglement is realized only with the simultaneous participation of all N of the constituent systems. The exponential increase with N in the amount of information required to describe the overall quantum system, while exceedingly beneficial for large-scale quantum information protocols[3], makes the task of classifying[209,210] and detecting such entangled states extremely difficult[40]. Still, there are prescribed methods to detect entanglement in select classes of multipartite states that generally rely on reconstructing the density matrix $\hat{\rho}$. Linear entanglement witnesses supplemented by tomography of $\hat{\rho}$ have been used to detect entanglement in six[275] and eight[276] atomic ions, as well as for hyper-entangled photons[277]. A serious drawback of quantum-state tomography is the prohibitive number of measurements and their accuracies that are required with increasing N.

In this chapter, I will focus on a specific class of quantum states in which exactly one photon is coherently shared among N distinct optical modes in the form of

$$|W\rangle = \frac{1}{2}[(|1000\rangle + e^{i\phi_1}|0100\rangle) + e^{i\phi}(|0010\rangle + e^{i\phi_2}|0001\rangle)], \tag{8.1}$$

shown here for $N = 4$, and with the relative phases ϕ, ϕ_1, ϕ_2 of the modes. This is a so-called W state, which plays an important role in quantum information protocols with photonic and matter qubits, as its entanglement is known to be robust against losses (e.g., tracing over a set of modes $K \leqslant N - 2$).

To detect entanglement for pure states in the form of Eq. 8.1 and their mixed state counterparts $\hat{\rho}_W$, we introduce the use of fundamental quantum uncertainty relations (see chapter 7). It has long been known for continuous variable systems that the uncertainty principle for non-commuting observables defines a boundary of measurement precision that can only be crossed by entangled states[278,279]. This observation has formed the basis of numerous Einstein-Podolsky-Rosen type experiments[280], including the unconditional teleportation[281]. For discrete variable systems as in Eq. 8.1, the uncertainty principle can be recast as a sum of uncertainties in certain physical observables that must always be greater than some minimum bound Δ_b for all unentangled states, whether pure or mixed (refs.[38,121], chapter 7).

As a first test of this novel concept, we created a bipartite entangled state analogous to $|W\rangle$. We verified the entanglement both by violation of an uncertainty relation[38] and by the well-established method of concurrence (refs.[27,34,37,178], see also chapters 2 and 4). The precise agreement of these two measurements over a wide range of parameter space attests to the reliability of uncertainty-based verification for entanglement of discrete variables (Figs. 8.1b and 8.2). We then extended our setup to create multipartite entangled states that coherently share a single photon among four optical modes and applied our verification protocol to them. Varying the phase coherence and the photon statistics of a candidate state $\hat{\rho}_W$ allowed us to explore the boundary between separable and entangled states, including those that separate four-fold, three-fold, and two-fold entanglement.

8.2 Nonlinear, nonlocal entanglement witness by way of quantum uncertainty relations

Our verification protocol is based on an exclusion principle for which N-mode entanglement can be unambiguously detected by simultaneously measuring physical observables $\{\hat{M}_i\}$ (projectors) with $i \in \{1, \ldots, N\}$ more precisely than is possible with only $(N-1)$-mode entangled states and their mixtures[38,121]. Specifically, we consider a sum uncertainty relation $\Delta = \sum_{i=1}^{N} \langle \hat{M}_i^2 \rangle - \langle \hat{M}_i \rangle^2 = 1 - \sum_{i=1}^{N} \langle \hat{M}_i \rangle^2$, and its lower bound $\Delta_b^{(K)}$, which is obtained for the one photon subspace of all states with at most $K < N$ mode entanglement. For any K-mode entangled state the inequality $\Delta \geq \Delta_b^{(K)}$ holds; therefore a violation of this inequality serves

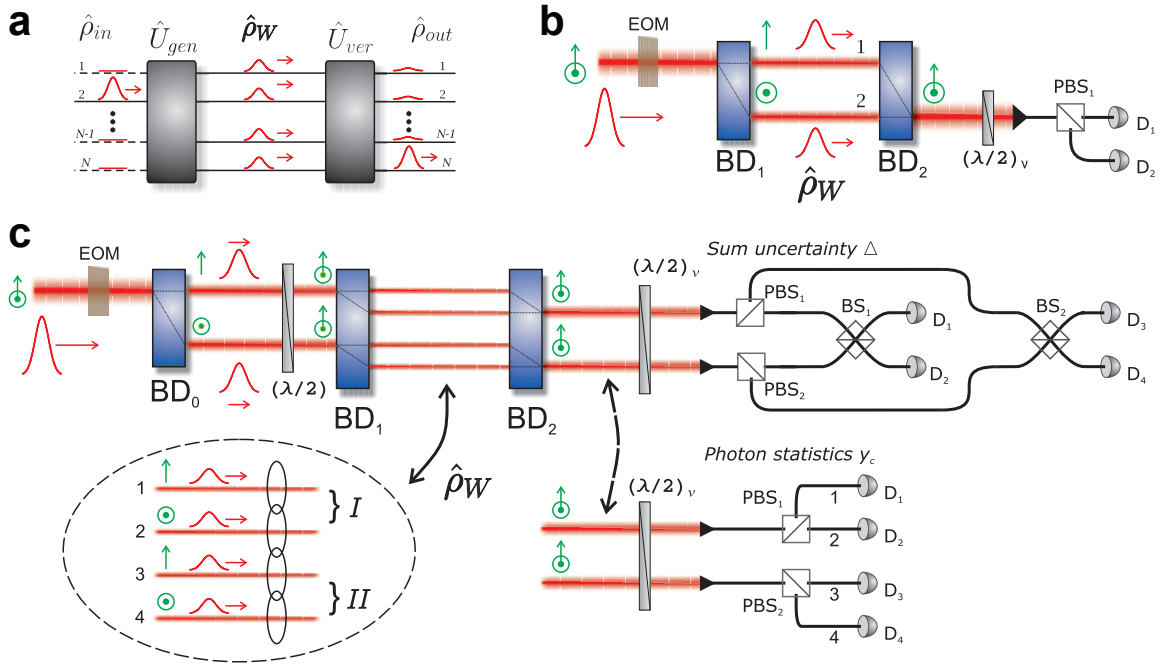

Figure 8.1: **Diagram of our entanglement generation and verification setups. a**, A single-photon pulse is transformed from a single input into an N-mode entangled state by $\hat{U}_{\text{gen}}$, and entanglement is verified with the operation $\hat{U}_{\text{ver}}$. **b**, Details of the setup for bipartite entanglement. Single photons are coherently split to occupy the two modes defined by the interferometer BD_1–BD_2 with the relative phase ϕ of $\hat{\rho}_W$ controlled by the EOM. By setting the waveplate $(\lambda/2)_{\text{v}}$ at 0°, the occupation of the individual modes is detected at D_1 and D_2, and we obtain the two-photon components of $\hat{\rho}_W$. With a setting of $(\lambda/2)_{\text{v}}$ at 22.5° single photon interference occurs at PBS_1, from which we obtain Δ; see also Fig. 8.2A. **c**, Details of the setup to create and verify quadripartite entanglement. The sequence of beamsplitters BD_0 and BD_1 generate the optical modes 1–4 which share a single photon. To measure Δ, we jointly optimize the relative phases in the verification interferometers for interferences at $\text{PBS}_{1,2}$ ($(\lambda/2)_{\text{v}}$ at 22.5°) and $\text{BS}_{1,2}$ to minimize the photon probability of all but one output mode. Here switching between measurements of Δ and y_c requires the indicated reconfiguration of fiber-optic components.

as a sufficient condition for genuine N-mode entanglement (see section 7.3). The projective operators are $\{\hat{M}_i\} = \{|W_i\rangle\langle W_i|\}$ with

$$\begin{aligned}
|W_1\rangle &= \tfrac{1}{2}(|1000\rangle + e^{i\beta_1}|0100\rangle + e^{i\beta_2}|0010\rangle + e^{i\beta_3}|0001\rangle) \\
|W_2\rangle &= \tfrac{1}{2}(|1000\rangle - e^{i\beta_1}|0100\rangle - e^{i\beta_2}|0010\rangle + e^{i\beta_3}|0001\rangle) \\
|W_3\rangle &= \tfrac{1}{2}(|1000\rangle - e^{i\beta_1}|0100\rangle + e^{i\beta_2}|0010\rangle - e^{i\beta_3}|0001\rangle) \\
|W_4\rangle &= \tfrac{1}{2}(|1000\rangle + e^{i\beta_1}|0100\rangle - e^{i\beta_2}|0010\rangle - e^{i\beta_3}|0001\rangle)
\end{aligned} \tag{8.2}$$

for the case of $N = 4$, and with phases $\{\beta_j\}$ where $j \in \{1, 2, 3\}$. They are optimally sensitive to entanglement, for particular settings of β_j, since the entangled state $|W\rangle$ in Eq. 8.1 is the only simultaneous eigenstate of all projective operators $\hat{M}_i$ (ref.[38], chapter 7).

In our work, the purported N-mode entangled state ($\hat{\rho}_W$) analogous to $|W\rangle$ is generated via the operation $\hat{\rho}_{\text{in}} \xrightarrow{\hat{U}_{\text{gen}}} \hat{\rho}_W$ (Fig. 8.1a) on an input state $\hat{\rho}_{\text{in}}$. Similarly entanglement is verified with $\hat{\rho}_W \xrightarrow{\hat{U}_{\text{ver}}} \hat{\rho}_{\text{out}}$. We

implement $\hat{M}_i$ for the case of two (Fig. 8.1b) and four (Fig. 8.1c) optical modes using beamsplitters[282] and photodetectors. The limit $\Delta \rightarrow 0$ indicates a significant overlap of the state $\hat{\rho}_W$ with only one of the projectors $\hat{M}_i$. In particular, for any choices of ϕ, ϕ_1, ϕ_2 that define Eq. 8.1 and the three corresponding orthonormal states, our measurements of $\hat{M}_i$ would yield $\Delta = 0$ for optimal settings of the phases β_j. A small Δ corresponds to a large statistical imbalance in the event distribution of the output optical modes, with one mode strongly preferred over the others. Conversely, if the generated state contains a photon which occupies one mode, e.g. $|1000\rangle$, our measurements would yield $\Delta = 0.75$. Due to the presence of transmission losses and beamsplitter imbalances in our setups, the projectors $|W_i\rangle\langle W_i|$ evolve into mixed states with significant vacuum components, but genuine multipartite entanglement can still be robustly detected for $\hat{\rho}_W$ (ref.[38], see section 8.11).

To determine theoretically the boundaries $\Delta_b^{(K)}$ for N-mode entanglement, we calculate Δ for all possible admixtures of states containing at most $K = N - 1$ mode entanglement. The presence of more than one excitation in $\hat{\rho}_W$ may allow significant overlap of its one-photon subspace with $|W\rangle$ (chapter 7), leading to a spurious detection of entanglement. Therefore, it is necessary to determine the contamination of the state $\hat{\rho}_W$ due to multiple excitations. By invoking local filtering operations, we are justified in confining our analysis to the reduced density matrix $\hat{\rho}_W^{(r)} = p_0\hat{\rho}_0 + p_1\hat{\rho}_1 + p_{\geq 2}\hat{\rho}_{\geq 2}$ which contains no more than one photon per mode, while still being guaranteed a lower bound of entanglement[27,110]. In our experiments, we measure the photon probabilities p_0, p_1, and $p_{\geq 2}$ that characterize the occupation of the vacuum subspace $\hat{\rho}_0$, the single-photon subspace $\hat{\rho}_1$, and the subspace containing multiple excitations $\hat{\rho}_{\geq 2}$. The degree of contamination due to more than one excitation is quantified by the parameter $y_c = 2(\frac{N}{N-1})\frac{p_2 p_0}{p_1^2}$, which is normalized to the case of independent and balanced coherent states for which $y_c = 1$. The observation of measurement uncertainty Δ below the threshold $\Delta_b^{(K)}$ together with a determination of y_c, then, manifestly confirms the presence of genuine $(K+1)$-mode entanglement.

8.3 Experimental procedure

Our experimental starting point is the generation of heralded single photons via Raman transitions in an optically dense atomic ensemble of cesium atoms[4] (section 8.8). Two-mode entangled states are created by coherently splitting a single photon into parallel modes with beamdisplacer BD_1 (Fig. 8.1b); the modes' relative phase, analogous to ϕ in Eq. 8.1, is controlled by an electro-optic modulator (EOM). The spatially separated modes are recombined at BD_2 and coupled into a single-mode optical fiber, with each mode encoded in the polarization bases $|H\rangle$ and $|V\rangle$. Achieving entanglement requires a constant relative phase of the optical modes. Absent any fluctuating drive voltage on the EOM, the beamdisplacer pair BD_1–BD_2 forms a passively stable interferometer (refs.[34,36], chapter 3). By driving the EOM with a randomly oscillating voltage, the phase coherence of the modes is destroyed, and any entanglement between them is lost. This setup provides a calibrated tool to explore the boundary between separable and entangled states.

8.4 Characterization of bipartite entanglement by concurrence and uncertainty relations

Following the generation of bipartite states, we search for the signatures of entanglement using our verification protocol. To measure Δ, we rotate the polarizations of both modes by 45° and interfere them with a polarizing beamsplitter (PBS_1). We record the photoelectric detection events at single-photon counters D_1 and D_2, and convert them to the normalized joint photon probabilities P_{ij} (i.e., i photons for mode 1 and j for mode 2). Varying the relative phase of the modes after they exit BD_2 produces the interference fringes shown in the inset to Fig. 8.2a (corresponding to P_{10} and P_{01}), which allow us to identify the minimum value of Δ supported by the modes for a given y_c. In particular, the sum uncertainty Δ is related to the fringe visibility V by $\Delta = \frac{1}{2}(1 - V^2)$. When the relative phase β between modes $1, 2$ is either 0° or 180°, we obtain a value of Δ as small as 0.006, which corresponds to a visibility of 99.4% (section 8.10). To measure the two-photon suppression of $\hat{\rho}_W$, we detect the individual modes and record the time series of all relevant coincidence events (i.e., P_{ij} with $i + j = 0, 1,$ or 2). Based on a calibration of the transmission from the face of BD_2 to the detectors, we infer the photon probabilities that determine y_c (section 8.9). We control y_c via the pump intensity for Raman transitions in the source ensemble (section 8.8, chapter 2).

8.4.1 Scaling behavior of concurrence and uncertainty relations for bipartite entanglement

We have explored bipartite entanglement verification in our system by varying both the phase coherence and the two-photon suppression of $\hat{\rho}_W$. Fig. 8.2a shows the dependence of Δ on the amplitude $\delta\phi$ of phase noise produced by the EOM. These results were obtained with two-photon contamination $y_c = 0.063 \pm 0.011$ such that entanglement is detected when $\Delta \lesssim 0.46$. With $\delta\phi = 360^\circ$, we expect the fringe visibility to be minimized, and therefore $\Delta = 0.5$. As $\delta\phi$ decreases below 270°, the statistics of our measurements become sufficiently imbalanced that the presence of entanglement is manifest. Absent any phase noise in the state generated at BD_1 (i.e., $\delta\phi = 0$), we obtain $\Delta \leq 0.03$ over a wide range of y_c as shown in Fig. 8.2b. The first-order coherence of our single-photon source and the phase stability of our apparatus guarantee $\Delta \approx 0$. The boundary in Δ between fully separable states and those that contain entanglement, $\Delta_b^{(1)}$, depends primarily on y_c through the relationship $\Delta_b^{(1)} = \frac{1}{2}(1 - y_c)$. Given the uncertainty of our measurements, of which the largest contribution is counting fluctuations in y_c, all of the states created with $y_c \leq 0.86$ verifiably contain bipartite entanglement.

A rigorous correspondence exists between our uncertainty verification protocol (for two modes) and concurrence, a measure of bipartite entanglement[178] (section 8.10). As a tool to understand the dependencies of the sum uncertainty and as a secondary confirmation of two-mode entanglement, we inferred the normalized concurrence $C_N = V - \sqrt{y_c}$ from our measurements of Δ (section 8.10). Using previously introduced rela-

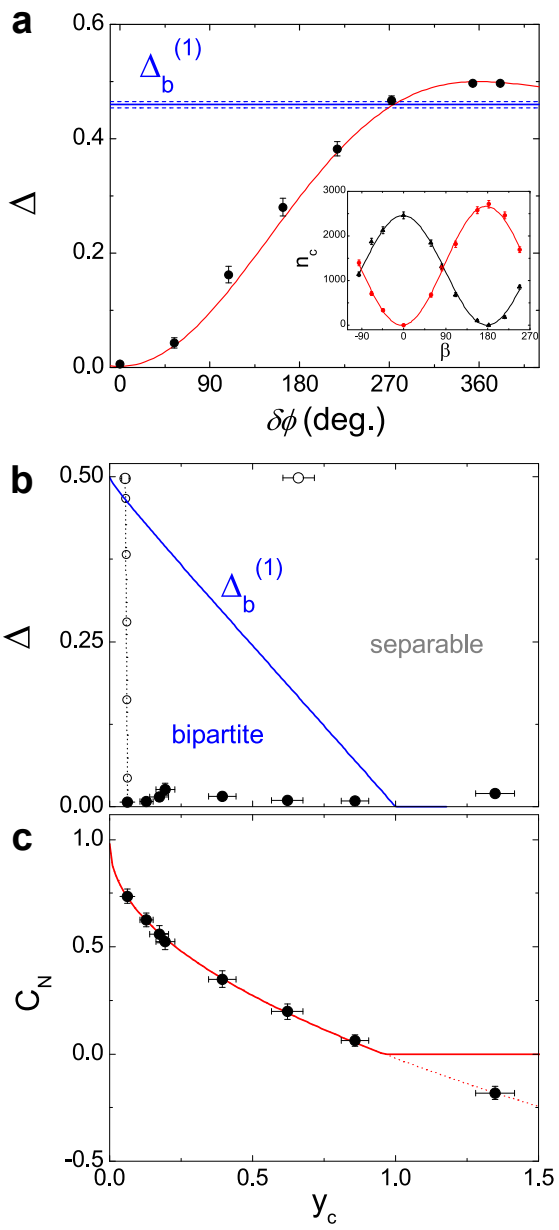

Figure 8.2: **Detection of entanglement between two optical modes using uncertainty relations. a**, The sum uncertainty Δ as a function of peak-to-peak phase noise $\delta\phi$ in the generated state $\hat{\rho}_W$. The solid blue line gives the boundary, $\Delta_b^{(1)}$, between entangled and separable states. The dotted lines indicate the range of $\Delta_b^{(1)}$ values that result from the uncertainty in our measurements of y_c. The red line is a fit to the data based upon a uniform distribution of phase noise. (Inset) Number of photons detected n_c in the output modes for a measurement time of 250 s as the relative phase β of the verification interferometer is varied. At minima and maxima of n_c we obtain $\Delta = 0.01$. **b**, Measured sum uncertainty with $\delta\phi = 0$ (filled circles) and boundary $\Delta_b^{(1)}$ (blue line) as a function of two-photon suppression. Data with $y_c < 1.0$ demonstrate entanglement of the two modes. By varying $\delta\phi$ from 0° to 360° (open circles), the modes' phase coherence is reduced, resulting in a loss of entanglement for $\delta\phi \gtrsim 270°$. **c**, Concurrence C_N (filled circles) inferred from measurements of Δ and the boundary $\Delta_b^{(1)}$. The solid line shows a theoretical prediction of concurrence ($\max(C_N, 0)$) based on an independent measurement of V and $p_1 = 0.22 \pm 0.02$. All the error bars in this figure represent standard deviations.

tionships, we can reformulate it as $C_N = \sqrt{1-2\,\Delta} - \sqrt{1-2\,\Delta_b^{(1)}}$. The inferred concurrence data shown in Fig. 8.2c demonstrate an increasing C_N, therefore a larger degree of entanglement, as we decrease y_c. Importantly, this behavior is in excellent quantitative agreement with our theoretical expectation for concurrence based upon quantum-state tomography[27,34]; this validates the use of uncertainty relations for entanglement verification (see Fig. 8.8 in section 8.10).

8.5 Experimental realization of multipartite entangled state for one photon

We now describe our investigation of multipartite entanglement with a single photon shared among four optical modes (Figs. 8.3 and 8.4). To generate four-mode entangled states we use the setup shown in Fig. 8.1c. A third beamdisplacer (BD_0) is added to the two-mode setup immediately before BD_1; it coherently splits a single photon polarized at 45° into two modes. In this case, the space between BD_1 and BD_2 supports four independent modes of $\hat{\rho}_W$ (composed of pairs I and II) that share a single photon. The EOM influences only the relative phase of the two pairs I, II, labeled ϕ in Eq. 8.1, leaving intact their individual phase coherence, and it provides a means to induce dephasing between the I, II pairs. The four spatially separated modes in the state $\hat{\rho}_W$ are combined into two separated spatial modes (each carrying the two modes encoded via the polarizations $|H\rangle$ and $|V\rangle$) that exit BD_2 and are coupled into single-mode fibers.

Measurements of Δ are performed by rotating the polarizations of all the modes by 45°, and pairwise interfering them with the network of four cascaded beamsplitters shown in Fig. 8.1c. We record all photoelectric events from detectors $\{D_1, ..., D_4\}$, but employ only events with a single photodetection for the determination of Δ (section 8.9). In this case, Δ depends jointly on the fringe visibilities of all four interferometric outputs. While BD_1 and BD_2 still guarantee long-term interferometric stability for the two pairs of modes I and II, the relative phases between other pairs are actively stabilized with respect to a laser that shares the same path. With the stabilization laser off, we apply calibrated feed-forward signals to the servo electronics, which transiently optimize the setup for measurements of various phase dependencies of Δ, including its global minimum (section 8.8). To extract y_c for the separated modes $1-4$, we insert the "photon statistics" setup at the location indicated in Fig. 8.1c, and we ensure that no interference occurs at PBS_1 and PBS_2 by setting the polarizations to the eigenaxes of the respective PBS. We obtain a record of the sixteen photon probabilities P_{ijkl} that determine y_c, with indices $i, j, k, l \in \{0, 1\}$ (section 8.9).

8.5.1 Scaling behavior of uncertainty relations for multipartite entanglement

8.5.1.1 Decoherence of multipartite entanglement induced by phase noise

Using sum uncertainty relations (refs.[38,121], chapter 7), we have unambiguously detected the presence of full four-mode entanglement in a photonic W state. Naturally, since $N > 2$, entanglement may be found amongst

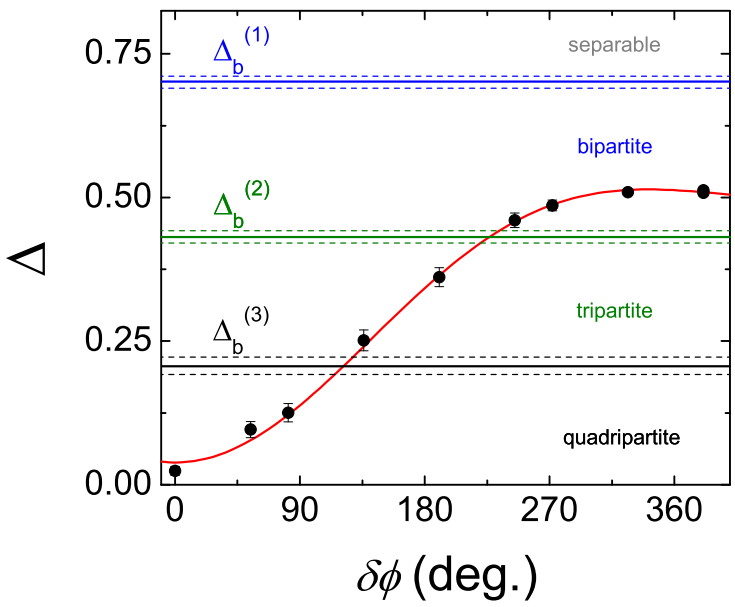

Figure 8.3: **Dependence of sum uncertainty Δ on the amplitude of phase noise $\delta\phi$ in the state $\hat{\rho}_W$.** These data were acquired with an approximately constant y_c in the range $0.06 - 0.08$; under these conditions $\Delta \lesssim 0.2$ demonstrates genuine four-mode entanglement. The horizontal lines indicate the boundaries $\Delta_b^{(K)}$ for entanglement. Here, the uncertainty of each boundary $\Delta_b^{(K)}$ (dashed lines) corresponds to the observed fluctuations in y_c. The red line is a fit to the data based on a model including a uniform distribution of phase noise.

not only the full set of modes, but bipartite and tripartite entangled states exist within a subset of them. A crucial feature of our verification protocol is that it clearly defines boundaries that distinguish between states with $\{N, N-1, \cdots, 2\}$ mode entanglement. As in the case with $N = 2$, the boundaries for $N = 4$ exist within the parameter space defined by Δ and y_c. To understand how the multipartite entanglement is affected by the phase coherence of $\hat{\rho}_W$, we introduce phase noise $\delta\phi$ over the range $0^\circ - 360^\circ$ between the two pairs of modes. Fig. 8.3 shows Δ as a function of $\delta\phi$ and the theoretical boundaries for two-, three-, and four-mode entanglement. For $\delta\phi \leqslant 225^\circ$, our verification protocol confirms the presence of genuine multipartite entanglement for three and four modes. Owing to the fact that dephasing is induced among only two pairs, the measured sum uncertainties do not exceed the threshold ($\Delta_b^{(1)} = 0.7$) defined by fully separable states[a]. A primary feature of multipartite W states is their resilience against phase noise, evidenced by the fact that the state which results from tracing over two modes in Eq. 8.1 still remains two-mode entangled[283]. This property of $|W\rangle$ explains our observation of entanglement even in the face of complete dephasing between the pairs I and II with 360° of phase noise.

[a]While there is a bipartite split between the pairs I and II (due to complete dephasing ϕ), we cannot unambiguously locate the bipartite split from the measurements presented in Fig. 8.3, as our verification protocol involves collective measurements on all four modes (section 7.3). In addition, note that we reserve the term, *genuine* N-partite entanglement, for states which can only be written in a pure-state decomposition of N-partite entangled states, thereby excluding the weaker condition of "N-partite entanglement" for mixtures of $M < N$ partite states along all possible bipartitions (i.e., a N-partite entangled state which does not have a physical split).

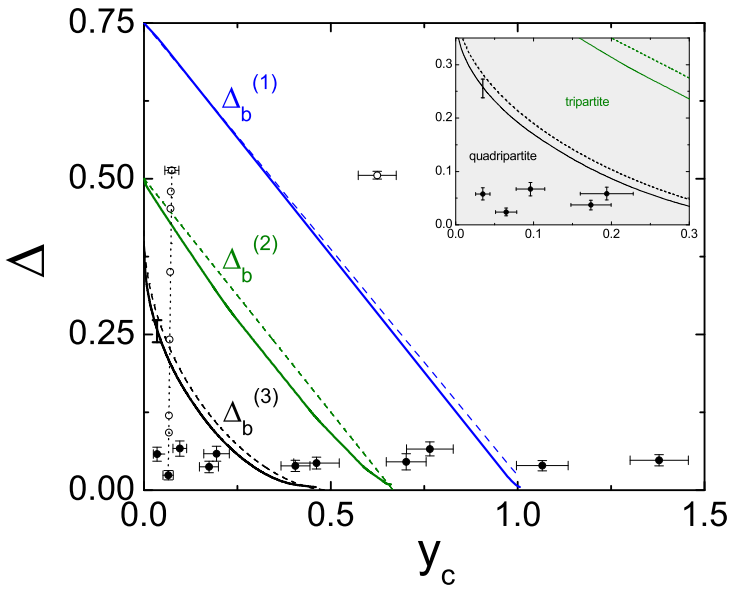

Figure 8.4: **Statistical transition of multipartite entanglement.** Sum uncertainty Δ as a function of two-photon suppression for $\delta\phi = 0°$ (closed circles) and $\delta\phi = 0°$–$360°$ (open circles). Solid lines indicate the boundaries between separable, bipartite, and tripartite entangled states for the parameters of our experiment. To understand the sizes of boundary corrections from the ideal case, the dashed lines show $\Delta_b^{(K)}$ for the ideal balanced and lossless case. The error bar on $\Delta_b^{(3)}$ indicates the statistical uncertainty in the boundary (section 8.11). (Inset) An expanded view of the quadripartite sector.

8.5.1.2 Statistical transition of multipartite entanglement

We have also explored the transitions from fully separable to bipartite ($K = 1$), tripartite ($K = 2$), and quadripartite ($K = 3$) entangled W states by measuring the sum uncertainty as a function of two-photon suppression y_c, with our results presented in Fig. 8.4. With $\delta\phi = 0$, we obtain a uniformly low $\Delta \leq 0.08$ over a range in y_c from $0.035 - 1.37$. These values of Δ are larger than in the two-mode case (Fig. 8.2b), and are explained by a small imbalance in $\hat{\rho}_W$ and by imperfections in the entanglement verification interferometers. Furthermore, these imperfections play an important role in the determination of the boundaries $\Delta_b^{(K)}$ for entanglement. As detailed in section 8.11, small imbalances in the beamsplitter ratios of PBS_1, PBS_2 and BS_1, BS_2 in Fig. 8.1c, and non-balanced transmission losses lead to displacements of the boundaries toward smaller $\{\Delta, y_c\}$. To reduce these boundary corrections, the beamsplitter ratios were all matched to $50\%/50\%$ to less than 3%, and the difference in losses of corresponding free-space and in-fiber optical paths were always held to less than 4%. Fig. 8.4 shows the sizes of the corrections by displaying the boundaries $\Delta_b^{(K)}$ for the ideal lossless and balanced case as dashed lines.

8.6 Advantage of multipartite entanglement verification via uncertainty relations

In comparison to quantum-state tomography, our multipartite verification protocol features an exponential reduction in the number of measurements required to unambiguously detect entanglement. Specifically, our protocol requires us to determine 2^4 elements of $\hat{\rho}_W^{(r)}$ for y_c and 4 elements of $\hat{U}_{\text{ver}}^{\dagger}\,\hat{\rho}_W^{(r)}\,\hat{U}_{\text{ver}}$ for Δ, a total of 20 elements out of the $4^4 = 256$ that comprise the reduced density matrix $\hat{\rho}_W^{(r)}$. Our protocol inherently features the use of nonlocal measurements $\hat{M}_i$, thereby requiring only two unique experimental steps to measure all necessary elements and unambiguously detect entanglement in $\hat{\rho}_W$. Furthermore, the nonlinear structure of Δ allows the simultaneous detection of all possible realizations of Eq. 8.1 (refs.[38,40]). These features alleviate the need for any complicated mechanism to control the measurement basis, which can be a challenge in tomography experiments[277] and other local-measurement-based verification protocols for $\hat{\rho}_W$. Although linear witnesses might also enable entanglement detection with less than full knowledge of $\hat{\rho}_W$ obtained from a few experimental steps[260], the unambiguous verification of entanglement requires robustness in the face of experimental imperfections, including multiple excitations and losses (section 8.11).

8.7 Conclusion

Our study has introduced a new technique for the unambiguous verification of multipartite W states. Specifically we examined entanglement in heralded quantum states specified by $\hat{\rho}_W$ with $N = 2, 4$. Entanglement detected with our protocol refers to that of the complete density matrix $\hat{\rho}_W$ presented to our verification system, and not to fictitious components deduced via post selection[110]. An extension of our protocol to different mode entangled states (requiring increased experimental resources) is discussed in chapter 7 (ref.[38]). Photonic entanglement, such as generated here, can be coherently mapped into atomic memories by way of electromagnetically induced transparency[30] for scalable quantum networks (chapter 6).

8.8 Experimental details

8.8.1 Ensemble-based single-photon source

The first step in our experiment is the conditional generation of single photons based on the proposal by Duan, Lukin, Cirac, and Zoller (*DLCZ*) (refs.[4,226]). In this protocol, heralded single photons are generated from excitations stored within an atomic ensemble. Single photon sources based upon atomic ensembles have been studied extensively; see refs.[74–76,79,82] for in-depth information. Here, we briefly present the experimental details relevant to our investigations.

We implement the *DLCZ* protocol with a cloud of $\sim 10^6$ cesium atoms that are collected using a magneto-

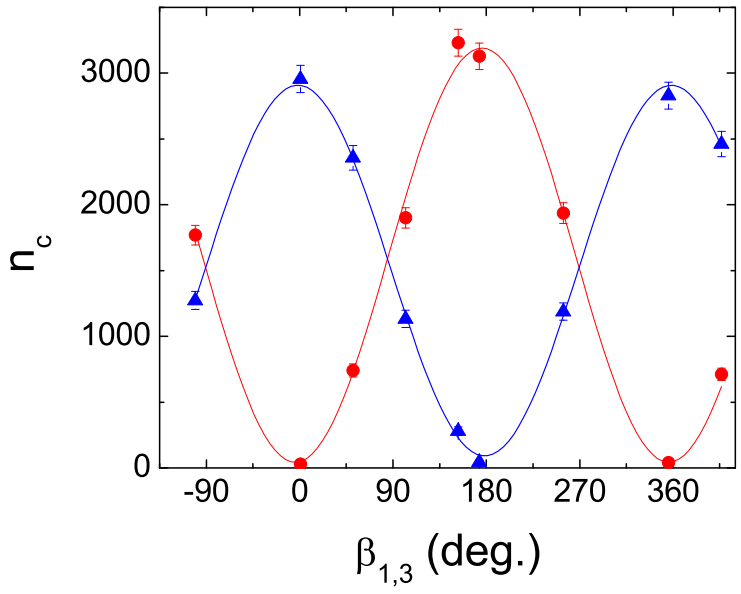

Figure 8.5: **Interference fringe in the four-mode sum uncertainty setup.** Number of detected photons n_c in output mode 1 (blue triangles) and output mode 2 (red circles) are plotted as a function of the phase $\beta_{1,3}$. Here a fringe visibility in excess of 99% and wide tunability of $\beta_{1,3}$ demonstrate the experimental capabilities necessary for measurements of Δ.

optical trap (MOT). Periodically, at a rate of 40 Hz, we switch off the trapping lasers and the magnetic field for the MOT, and we prepare all the atoms into the $F = 4$ hyperfine manifold ($6^2S_{1/2}$) of Cs. After waiting 3 ms for the MOT fields to decay, we begin a series of ≈ 6400 trials, each with a period of 625 ns. To begin each trial, we illuminate the cloud with a weak near-resonant "write" laser pulse which excites a Raman transition with low probability for a collective mode of the ensemble. The success of this process is heralded by a Raman scattered single photon that is correlated with the presence of an atomic excitation. By way of a many-atom cooperative enhancement [70,226], the atomic excitation can be efficiently converted into a single photon in a well-defined spatial mode with the application of an intense "read" pulse. This heralded single photon forms the basis of this experiment described in this chapter.

We have studied the characteristics of our single photon source in detail [75,76]. Importantly, the two-photon suppression, $y_c = 2(\frac{N}{N-1})\frac{p_2 p_0}{p_1^2}$, where N is the number of optical modes, of the purportedly entangled state $\hat{\rho}_W$ depends critically on the presence of multiple collective excitations within the ensemble (i.e., the single-photon source). The relative probability of a trial that has multiple ensemble excitations to a trial that has a single excitation can be suppressed by reducing the write laser intensity. Therefore, we can exercise full control over y_c of the quantum state $\hat{\rho}_W$ by way of a tunable write laser intensity. Furthermore, we can understand the efficiency of heralded single-photon generation. After accounting for detector and transmission losses, we estimate that the efficiency of the read-out process in our experiments is $\approx 50\%$. This leads to a single-photon probability of $p_1 \approx 20\%$ ($p_1 \approx 10\%$) in our two-mode (four-mode) experiments for the entangled state $\hat{\rho}_W$ in Fig. 8.1.

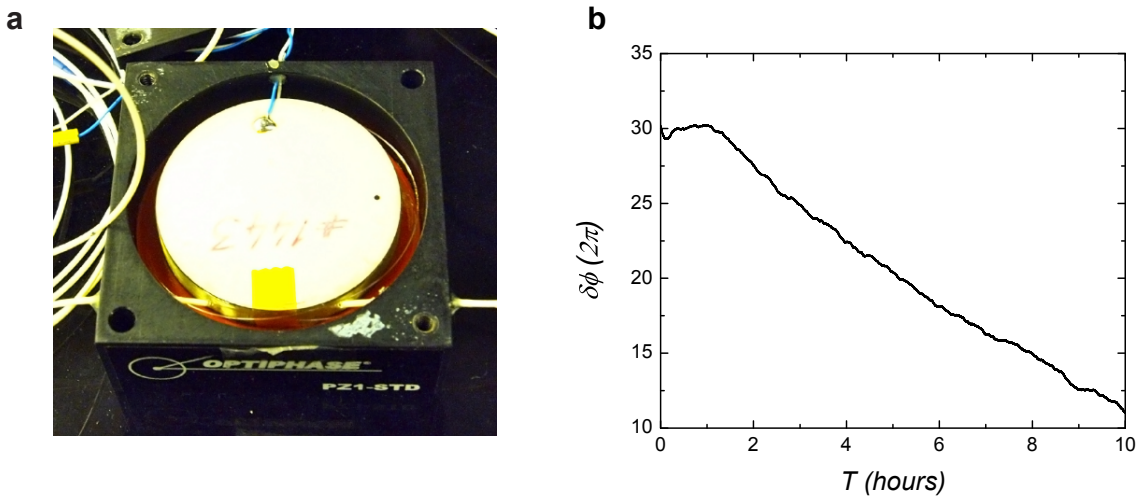

Figure 8.6: **A high-bandwidth fiber stretching module. a**, Inside the fiber stretching module (Optiphase), PM fiber is mounted on a circular disc piezoelectric transducer (PZT), which has a sharp mechanical resonance around $\simeq$ 55 kHz. The breathing mode of the PZT element is used to phase-modulate the fiber at $\sim$ 100 kHz (above the first resonance). Two lock-in amplifiers (DSP lock-in amplifiers, SRS 830 and 510) are used to generate an error signal by modulation spectroscopy on the interferometers in Fig. 8.1. The output of the locking servo described in Appendix A is fed into a high-voltage amplifier (Burleigh, PZ-70) to drive the fiber stretcher. At 1 kV, we estimated the reduction of polarization extinction ratio for the PM fiber from 30 dB to 20 dB, due to spurious stress-induced birefringence. **b**, Dynamic range of the active phase stabilization scheme via fiber stretchers. Thanks to the high dynamic range (up to $\delta\phi \sim 50 \times 2\pi$ at 852 nm) of the fiber stretchers, we can set the interferometer to a certain value of phase over several days without needing to re-lock the interferometer (mainly limited by the stability of the reference laser).

8.8.2 Phase stabilization

The generation and verification of entanglement in our experiments require that the relative phases of the purportedly entangled optical modes in Fig. 8.2 be stable (the various phase factors that describe the state $|W\rangle$ are shown in Eq. 8.1). As described in section 8.3, our experiments with two-mode entanglement (Fig. 8.2a) feature passive stability of the modes' relative phase $\beta_{1,2}$, guaranteed by the Mach-Zehnder interferometer formed with a pair of beamdisplacers BD_1–BD_2 (ref.[34], chapter 3). These beamdisplacers are birefringent crystals which separate an input state into two parallel modes based on its polarization. Therefore, the two displacers support a pair of interferometrically stable modes, which are encoded in $|H\rangle$ and $|V\rangle$.

However, for our quadripartite entanglement experiments (Fig. 8.1c), the beamdisplacer pairs alone cannot define four spatially resolved stable optical modes. Therefore, we have devised a convenient method that combines passive stability and active stabilization. The beamdisplacers BD_1–BD_2 support four modes of which the relative phases of modes $\{1,2\}$ ($\beta_{1,2}$) and $\{3,4\}$ ($\beta_{3,4}$) are inherently stable. However, as is clearly visible in Fig. 8.1c, the relative phases of modes $\{1,3\}$ ($\beta_{1,3}$) and $\{2,4\}$ ($\beta_{2,4}$) depend on the independent paths through, for example, fiber-optic PBS_1 and PBS_2 (Fiber PBS from Oz Optics). By incorporating an auxiliary reference laser, E_{aux}, we can actively control the relative path lengths of the modes $\{1,3\}$ and $\{2,4\}$. Prior to BD_0 in Fig. 8.1c, we overlap the orthogonally polarized E_{aux} and the input mode ($\hat{\rho}_{\text{in}}$); the

frequency of E_{aux} is the same as the single photon's. To stabilize $\beta_{1,3}$ and $\beta_{2,4}$, we set $(\lambda/2)_{\text{v}}$ at 0° and create interference fringes at the outputs of BS_1 and BS_2. Phase-modulation spectroscopy allows us to lock the relative phases so that a high contrast interference ($V > 0.99$) is achieved for quantum fields (Fig. 8.5). The control of the relative path lengths for the modes, as well as their modulation, is afforded by piezoelectric fiber stretcher modules (Fig. 8.6a, see also Appendix A for the locking servo) located between PBS_1 and BS_1, and PBS_2 and BS_2, in Fig. 8.1c. These devices provide up to $50 \times 2\pi$ of dynamic range enabling the interferometers to remain continuously locked for several days (Fig. 8.6b).

Importantly, to avoid noise associated with the auxiliary laser in the single-photon detectors $\{D_1, \cdots, D_4\}$, E_{aux} must be filtered out. In our work, phase stabilization is performed asynchronously with entanglement generation and its verification in the fiber-based network of interferometers (Appendix A). This eliminates the need to wavelength filter E_{aux} as was necessary in previous experiments[27]. During the 21 ms of our 40 Hz experimental cycle that the MOT is activated, E_{aux} is switched on, the output modes of the sum uncertainty setup are directed toward an auxiliary set of detectors with MEMS fiber multiplexers (Sercalo), and our servo electronics stabilize $\beta_{1,3}$ and $\beta_{2,4}$. To prepare for measurements of Δ, we switch off E_{aux} and reroute the output modes to the single-photon detectors with the MEMS multiplexers, and we use dynamic polarization rotators (nematic liquid-crystal waveplates from Meadowlark[b]) to set $(\lambda/2)_{\text{v}}$ at 22.5°. Further, we apply calibrated feedforward signals to the servo electronics that can precisely scan the relative phases of modes $\{1, 3\}$ and $\{2, 4\}$ to explore the dependencies of our Δ measurements. Fig. 8.5 shows the number of photons (n_c) detected at D_1 and D_2 as a function of $\beta_{1,3}$. Here, all other relevant optical phases in our setup were optimized to achieve minimum Δ. Therefore, at the minima and maxima of n_c corresponding to $\beta_{1,3} = 0,\ 180^\circ,\ 360^\circ$, we find that Δ is 0.06 ± 0.01.

8.9 Inference of the photon probabilities for obtaining y_c and Δ

Our entanglement verification protocol requires that we characterize the photon probabilities of the sum uncertainty output modes and those of modes 1–4 that comprise the state $\hat{\rho}_W$. We infer these photon probabilities from a time record of photodetection events obtained with single photon counters placed at the outputs of the relevant modes. Based upon independent measurements of the transmission losses to the photodetectors, we determine the photon probabilities[193]. Specifically, for measurements of y_c we obtain a set of sixteen probabilities that characterize the diagonal elements of the reduced density matrix $\hat{\rho}_W^{(r)} = p_0\hat{\rho}_0 + p_1\hat{\rho}_1 + p_{\geq 2}\hat{\rho}_{\geq 2}$. The diagonal elements are P_{ijkl} where the index $i = \{0, 1\}$ is for finding zero or one photon in mode 1 of $\hat{\rho}_W$, $j = \{0, 1\}$ in mode 2, and so on for k, l in modes 3 and 4 (Fig. 8.1c). The vacuum subspace of $\hat{\rho}_W^{(r)}$ is characterized by the term $p_0 = P_{0000}$. Four elements comprise the one-photon subspace, $\hat{\rho}_1$, via

[b] Bandwidth of the liquid-crystal (LC) waveplates is slow (only $\sim$ 1 kHz) compared to that of Pockels cells, which was still suitable for our purpose. In addition, since these are biaxial nematic devices, there are only two stable positions whereby the eigenaxes of the crystal could align[284]. However, one advantage is that the LC only requires a modest amount of voltage (< 5 V) to set the fast axis of the crystal to the predetermined direction.

$p_1 = P_{1000}+P_{0100}+P_{0010}+P_{0001}$. Likewise, 11 elements comprise the subspace with two or more photons, $\hat{\rho}_{\geq 2}$, subject to the restriction of one photon per mode, with $p_{\geq 2} = P_{1100}+P_{1010}+\cdots+P_{1110}+\cdots+P_{1111}$. In the case of y_c measurements, the typical detection efficiency including the photodetector quantum efficiency is $\approx 20\%$. To infer the photon probabilities at the outputs of the verification interferometers (Fig. 8.1c) for our measurements of Δ, we follow a similar procedure, but we confine our analysis to the subspaces $\hat{\rho}_0$ and $\hat{\rho}_1$. In this case, the typical photon detection efficiency is $\approx 30\%$.

Similarly, due to the uses of photon non-resolving photodetectors and lossy paths for our projectors (Eq. 8.2), the measured sum uncertainty Δ_{m} includes spurious contributions from multiple photons $p_{\geq 2}$. To account for this, we follow the procedure described in section 7.6.2 (ref.[38], chapter 7), which leads to a conservative estimation of the photon sum uncertainty Δ arising only from $\hat{\rho}_1$. In the case of balanced losses, the correction factor c is expressed in terms of two-photon suppression y_c and transmission efficiency η with

$$c \approx (1 + \frac{3}{8}(2-\eta)p_1 y_c), \tag{8.3}$$

where we apply $c\Delta_m > \Delta$ to obtain a conservative estimate of the 1-photon Δ (section 7.6.2; see also chapter 9 for a more efficient method for obtaining the upper bound of Δ). For our experimental parameters, the correction factor $(c-1) \approx 6\%$ is obtained for $y_c = 1$, as depicted in black line of Fig. 8.7. This is significantly smaller than the fractional uncertainties $\frac{\delta(\Delta_m)}{\Delta_m} \approx 25\%$ of our data. Furthermore, since the correction factor scales as y_c, the correction factor gives $(c-1) < 1\%$ for the relevant data sets of $y_c < 0.2$ for four-mode entanglement (Fig. 8.4). Following the standard procedures for loss propagations[193], we also account for the effect of differential losses and imbalanced beamsplitter ratios (red line in Fig. 8.7).

8.9.1 Imbalances and threshold detectors

In chapter 7, we developed a method to account for losses and imbalances. Here, we obtain an explicit formulas of q_1 in the case of differential losses and imbalanced beamsplitter ratios. In order to propagate $\hat{\rho}_W^{(r)}$ through the imbalanced verification interferometers, we rewrite $\hat{\rho}_W^{(r)}$,

$$\hat{\rho}_W^{(r)} = p_0\hat{\rho}_0 + \hat{\rho}_1' + \hat{\rho}_2', \tag{8.4}$$

in terms of mode operators $\hat{a}_i$ where

$$\hat{\rho}_1' = \sum_{i,j} \frac{P_i + P_j}{2} V(i,j)\hat{a}_i^\dagger|\overline{0}\rangle\langle\overline{0}|\hat{a}_j \tag{8.5}$$

$$\hat{\rho}_2' = \sum_{j>i}^{4}\sum_{l>k}^{4} \frac{P_{ij} + P_{kl}}{2} V(ij,kl)\hat{a}_i^\dagger\hat{a}_j^\dagger|\overline{0}\rangle\langle\overline{0}|\hat{a}_k\hat{a}_l. \tag{8.6}$$

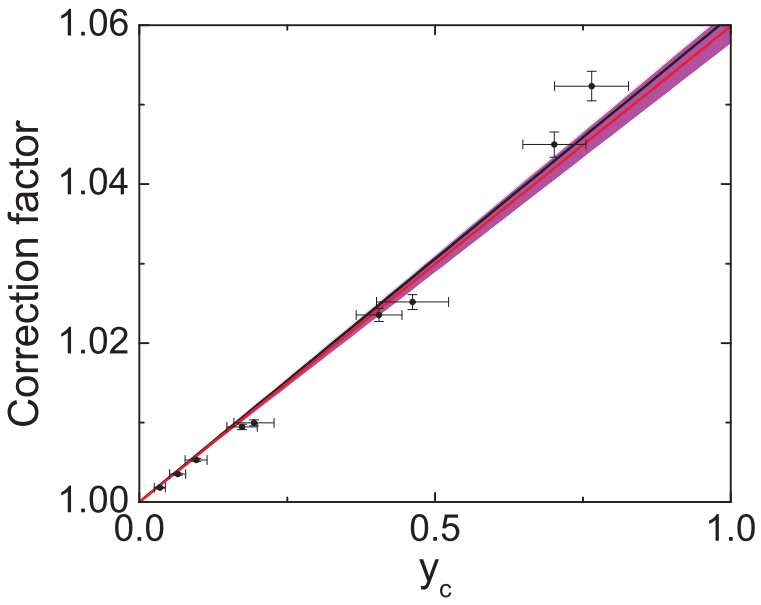

Figure 8.7: **Correction factor c as a function of two-photon contamination y_c.** The black line corresponds to the calculation of c for balanced losses $\eta = 36\%$ and fixed $p_1 = 9\%$. The red line is a calculation of c including differential losses $\{\eta\}$ and imbalanced beamsplitter ratios $\{\alpha\}$ (Table 8.1). The uncertainty of c due to the systematic uncertainties in $\{\eta, \alpha\}$ is shown as purple bands. The filled circles show c using the data points in the experiment (i.e., using the parameters P_{ijkl} of each points). The uncertainty in the vertical direction includes the systematic uncertainties in $\{\eta, \alpha\}$ as well as the statistical uncertainties in P_{ijkl}.

Here, $V(i,j) = V(j,i)$ and $V(i,i) = 1$. Through the lossy and imbalanced setup in Fig. 8.1, the mode operators $\hat{a}_i$ are transformed into following forms,

$$\hat{a}_i \mapsto \sum_{i'} e^{i\phi_{i'}^{(i)}} \sqrt{\alpha_{i'}^{(i)}} (\sqrt{\eta_{i'}^{(i)}} \hat{a}_{i'} + \sqrt{1-\eta_{i'}^{(i)}} \hat{v}_{i'}). \tag{8.7}$$

Here, $\hat{v}_{i'}$ is the vacuum mode operator. The precise correspondences between the imbalances $\{\alpha_{i'}^{(i)}, \eta_{i'}^{(i)}, \phi_{i'}^{(i)}\}$ and experimental parameters (Table 8.1 and Fig. 8.1) are not shown for clarity.

The state $\hat{\rho}_W^{(r)}$, then, is transformed to a state (see section 7.6.2 for the balanced case),

$$\hat{\rho}_\eta^{(r)} = p_0' \hat{\rho}_0 + p_1' (q_1' \hat{\rho}_1^{(1)} + (1-q_1') \hat{\rho}_1^{(2)}) + p_{\geq 2}' \hat{\rho}_{\geq 2}^{(2)}, \tag{8.8}$$

where the relevant parameters $\{p_1' q_1', p_1'(1-q_1'), p_2'\}$ are given as[c]

$$p_1' q_1' = \sum_{i,j} \frac{P_i + P_j}{2} V(i,j) \sum_\kappa e^{-i(\phi_\kappa^{(i)} - \phi_\kappa^{(j)})} \sqrt{\eta_\kappa^{(i)} \eta_\kappa^{(j)}} \sqrt{\alpha_\kappa^{(i)} \alpha_\kappa^{(j)}} \tag{8.9}$$

[c]Here, we have assumed that the two-photon subspace is fully coherent, $V(ij,kl) = 1$, thereby leading to $\Delta(\hat{\rho}_1^{(2)}) = \Delta(\hat{\rho}_2^{(2)}) = 0$ and a conservative estimate of Δ.

$$p_1'(1-q_1') = \sum_{i>j}\sum_{k>l}\frac{P_{ij}+P_{kl}}{2}\frac{1}{2}\sum_{\kappa_1,\kappa_2}\sqrt{\alpha_{\kappa_1}^{(i)}\alpha_{\kappa_2}^{(j)}\alpha_{\kappa_1}^{(k)}\alpha_{\kappa_2}^{(l)}}e^{-i(\phi_{\kappa_1}^{(k)}+\phi_{\kappa_2}^{(l)}-\phi_{\kappa_1}^{(i)}-\phi_{\kappa_2}^{(j)})}\times \\ (\sqrt{\eta_{\kappa_1}^{(i)}(1-\eta_{\kappa_2}^{(j)})}+\sqrt{\eta_{\kappa_2}^{(j)}(1-\eta_{\kappa_1}^{(i)})})(\sqrt{\eta_{\kappa_1}^{(k)}(1-\eta_{\kappa_2}^{(l)})}+\sqrt{\eta_{\kappa_2}^{(l)}(1-\eta_{\kappa_1}^{(k)})}) \tag{8.10}$$

$$p_{\geq 2}' = \sum_{i>j}\sum_{k>l}\frac{P_{ij}+P_{kl}}{2}\sum_{\kappa_1,\kappa_2}\sqrt{\alpha_{\kappa_1}^{(i)}\alpha_{\kappa_2}^{(j)}\alpha_{\kappa_1}^{(k)}\alpha_{\kappa_2}^{(l)}}e^{-i(\phi_{\kappa_1}^{(k)}+\phi_{\kappa_2}^{(l)}-\phi_{\kappa_1}^{(i)}-\phi_{\kappa_2}^{(j)})}\sqrt{\eta_{\kappa_1}^{(i)}\eta_{\kappa_2}^{(j)}\eta_{\kappa_1}^{(k)}\eta_{\kappa_2}^{(l)}}. \tag{8.11}$$

Therefore, correction factor $c = 1/q_1$ is given as (chapter 7)

$$q_1 = \frac{p_1'q_1'}{p_1'+p_{\geq 2}'}. \tag{8.12}$$

In the case of balanced losses η, it can be confirmed that Eqs. 8.3 and 8.12 are equivalent.

Here, we give the definitions of $\{\alpha_{i'}^{(i)}, \eta_{i'}^{(i)}, \phi_{i'}^{(i)}\}$ following the notations in Fig. 8.9.

$$\alpha_{i'}^{(i)} = \begin{pmatrix} \alpha_{14}'\alpha_{12} & \alpha_{14}'(1-\alpha_{12}) & (1-\alpha_{14}')\alpha_{34} & (1-\alpha_{14}')(1-\alpha_{34}) \\ \alpha_{23}'(1-\alpha_{12}) & \alpha_{23}'\alpha_{12} & (1-\alpha_{23}')(1-\alpha_{34}) & (1-\alpha_{23}')\alpha_{34} \\ (1-\alpha_{23}')(1-\alpha_{12}) & (1-\alpha_{23}')\alpha_{12} & \alpha_{23}'(1-\alpha_{34}) & \alpha_{23}'\alpha_{34} \\ (1-\alpha_{14}')\alpha_{12} & (1-\alpha_{14}')(1-\alpha_{12}) & \alpha_{14}'\alpha_{34} & \alpha_{14}'(1-\alpha_{34}) \end{pmatrix} \tag{8.13}$$

$$e^{i\phi_{i'}^{(i)}} = \begin{pmatrix} e^{i\phi_{i_1}} & e^{i\phi_{i_2}} & -e^{i\phi_{i_3}} & -e^{i\phi_{i_4}} \\ e^{i\phi_{i_1}} & -e^{i\phi_{i_2}} & -e^{i\phi_{i_3}} & e^{i\phi_{i_4}} \\ e^{i\phi_{i_1}} & -e^{i\phi_{i_2}} & e^{i\phi_{i_3}} & -e^{i\phi_{i_4}} \\ e^{i\phi_{i_1}} & e^{i\phi_{i_2}} & e^{i\phi_{i_3}} & e^{i\phi_{i_4}} \end{pmatrix} \tag{8.14}$$

$$\eta_{i'}^{(i)} = \begin{pmatrix} \eta_1\eta_1' & \eta_2\eta_1' & \eta_3\eta_4' & \eta_4\eta_4' \\ \eta_1\eta_2' & \eta_2\eta_2' & \eta_3\eta_3' & \eta_4\eta_3' \\ \eta_1\eta_2' & \eta_2\eta_2' & \eta_3\eta_3' & \eta_4\eta_3' \\ \eta_1\eta_1' & \eta_2\eta_1' & \eta_3\eta_4' & \eta_4\eta_4' \end{pmatrix} \tag{8.15}$$

8.10 Concurrence and bipartite uncertainty relations

For bipartite systems, there exist entanglement measures such as concurrence (*C*) and entanglement of formation (*EOF*) (ref.[178]), which range from 0 for a fully separable state to 1 for a maximally entangled state[110]. In Fig. 8.2, we quantitatively compared our method of entanglement verification with uncertainty relations to a theoretical calculation of concurrence based on a model in chapter 3 (ref.[34]). Here, we derive a relationship between concurrence and the degree that a measurement of the sum uncertainty violates the entanglement boundary, specified by the measured Δ and the uncertainty bound $\Delta_b^{(1)}$.

Following ref.[27], we find that the concurrence is given by $C = Vp_1 - 2\sqrt{p_0p_2}$ (chapter 3), where V corresponds to the fringe visibility when the two modes are interfered[27]. If we normalize the concurrence by the 1-photon probability p_1, we obtain

$$C_N \equiv \frac{C}{p_1} = V - \sqrt{y_c} \tag{8.16}$$

where $y_c = \frac{4p_2p_0}{p_1^2}$.

Let us first define the visibility V in terms of the measured Δ. We denote P_{10} (P_{01}) as the normalized probability of finding only 1 photon in the output mode 1 (2) (Fig. 8.2a) such that $P_{10} + P_{01} = 1$. The visibility is given as $V = |P_{10} - P_{01}|$. Similarly, the sum uncertainty is defined as $\Delta = 1 - (P_{10})^2 - (P_{01})^2$, which then yields,

$$V = \sqrt{1 - 2\Delta}. \tag{8.17}$$

We relate the two-photon contamination y_c to the uncertainty bound $\Delta_b^{(1)}$. In this way, we can understand the dependence of C_N on the degree for which the inequality $\Delta \geq \Delta_b^{(1)}$ is violated. In order to derive the uncertainty bound $\Delta_b^{(1)}$, we consider a separable state of the form,

$$|\Psi_{sep}\rangle = \frac{(|0_1\rangle + e^{i\phi_1}\sqrt{\varepsilon_1}|1_1\rangle)(|0_2\rangle + e^{i\phi_2}\sqrt{\varepsilon_2}|1_2\rangle)}{\sqrt{(1+\varepsilon_1)(1+\varepsilon_2)}} \tag{8.18}$$

with $p_0 = 1 - p_1 - p_2$, $p_1 = \frac{\varepsilon_1 + \varepsilon_2}{(1+\varepsilon_1)(1+\varepsilon_2)}$, $p_2 = \frac{\varepsilon_1\varepsilon_2}{(1+\varepsilon_1)(1+\varepsilon_2)}$, and the phases ϕ_1, ϕ_2. This state parameterizes all possible pure separable states, and mixed states can be accounted by arbitrarily mixing different pure states. For bipartite systems, however, the uncertainty bound for pure states is convex (Fig. 8.2b), and any mixing of the pure states increases the sum uncertainty [121]. Therefore, we only consider the cases for pure states, and we find

$$\Delta_b^{(1)} = \frac{1 - y_c}{2}. \tag{8.19}$$

By substituting Eq. 8.17 and 8.19 into Eq. 8.16, we obtain the relationship between concurrence and the violation of uncertainty bounds for a biseparable system, namely

$$C_N = \sqrt{1 - 2\Delta} - \sqrt{1 - 2\Delta_b^{(1)}}. \tag{8.20}$$

We emphasize the equivalence of the two verification protocols based on the violation of the uncertainty bound and the concurrence. The operational differences between the two entanglement verification protocols are the measurements of visibility (by varying the relative phase $\beta_{1,2}$) and the sum uncertainty Δ (with a fixed relative phase $\beta_{1,2}$). In Fig. 8.8, we compare the concurrence $C_N^{(\hat{\rho}_W)}$ directly measured via quantum state tomography [27] and the concurrence C_N inferred from violation of the uncertainty bound $\Delta_b^{(1)}$ (Fig. 8.2c). The precise correspondence of the two experimental results suggest that the underlying relationship between the two entanglement verification methods, as derived here (Eq. 8.20), is correct.

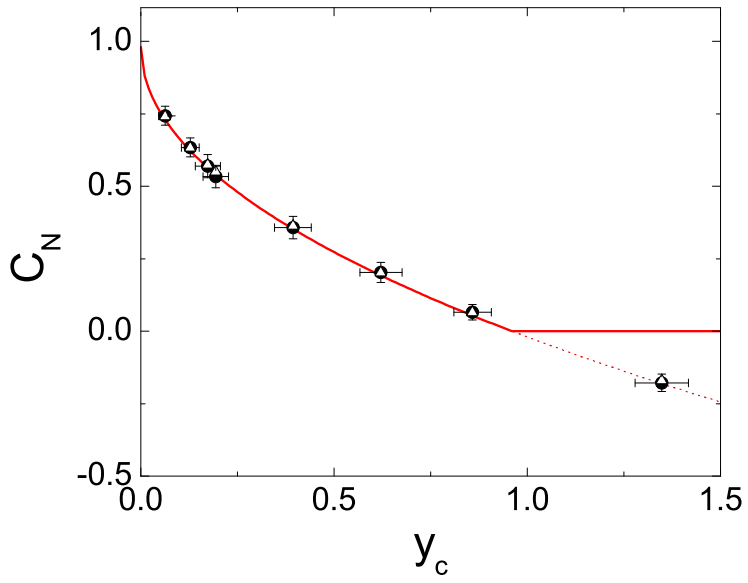

Figure 8.8: **Comparison between the directly measured concurrence and the inferred concurrence.** We compare the directly measured concurrence $C_N^{(\hat{\rho}_W)}$ (open triangles) based on quantum state tomography [27] and the concurrence C_N (filled circles) inferred from the measured degree of violation of the uncertainty bound specified with parameters $\{\Delta, \Delta_b^{(1)}\}$ (Fig. 8.2, Eq. 8.20). The red curve shows the theoretical prediction of concurrence as a function of the two-photon component y_c based on a model in ref. [34]. The errors in C_N reflect the 1σ-statistical uncertainties and the error bars for the measured concurrence $C_N^{(\hat{\rho}_W)}$ are not shown for clarity. The precise correspondence between $C_N^{(\hat{\rho}_W)}$ and C_N validates the use of Eq. 8.20.

8.11 Constructing the projective operators for the uncertainty relations

In the presence of transmission losses $\{\eta, \eta'\}$ and imbalanced beamsplitter ratios $\{\alpha, \alpha'\}$ in the verification interferometers shown in Fig. 8.9, the projectors no longer correspond to the pure state descriptions $\hat{M}_i = |W_i\rangle\langle W_i|$ in Eq. 8.2 (ref. [38], chapter 7). Using the standard technique for loss propagations and beamsplitter transformations [193], the original projectors $|W_i\rangle\langle W_i|$ become mixed states of the following form,

$$|W_i\rangle\langle W_i| \mapsto (1 - q_1^{(i)})|0000\rangle\langle 0000| + q_1^{(i)}|\Pi_i\rangle\langle\Pi_i|, \tag{8.21}$$

where $q_1^{(i)}$ gives the probability of a successful projective measurement in mode i for an entangled state $|\Pi_i\rangle$, $|0000\rangle\langle 0000|$ is the vacuum state, and $|\Pi_i\rangle\langle\Pi_i|$ is a pure state containing a single-photon shared among four optical modes (ref. [38], chapter 7). In the case of a conditional measurement (i.e., post-selecting the cases where we find a single-excitation among the four outputs of the cascaded beamsplitters in Fig. 8.1c), $|\Pi_i\rangle\langle\Pi_i|$ describes the projective measurement for the output mode i, $\hat{M}_i = |\Pi_i\rangle\langle\Pi_i|$. Unlike the original projectors $|W_i\rangle$ in Eq. 8.2, these projectors $|\Pi_i\rangle$ may not be orthogonal, but they span the single-photon subspace $\hat{\rho}_1$ of the physical state $\hat{\rho}_W$.

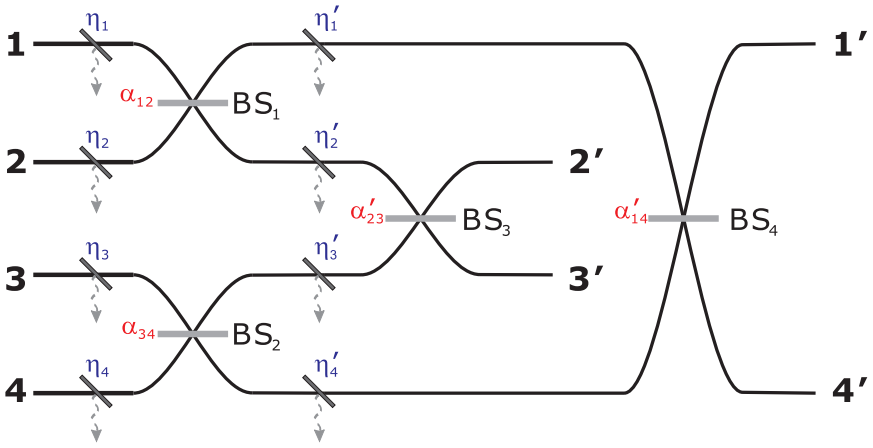

Figure 8.9: **A simplified setup for the verification protocol (sum uncertainty).** The setup includes differential transmission efficiencies $\{\eta, \eta'\}$ (blue) and imbalanced beam-splitter ratios $\{\alpha, \alpha'\}$ (red). The wiggly dashed arrows correspond to the auxiliary output modes which are traced over for loss propagation.

Generally, any imbalances (whether they are due to differential losses or beamsplitter ratios) in the verification interferometers cause reductions of the overlaps $|\langle W_i|\Pi_i\rangle|^2$ between projectors $|W_i\rangle$ and $|\Pi_i\rangle$, thereby making the protocol less sensitive to entanglement in $\hat{\rho}_W$ (ref.[38], section 7.6.1). In practice, the corrected bounds $\Delta_b^{(K)}$ always decrease towards smaller two-photon component y_c from the ideal lossless and balanced case, as shown for our experimental parameters $\{\eta, \eta'\}$ and $\{\alpha, \alpha'\}$ in Fig. 8.4. Furthermore, the uncertainties in the measurement of $\{\eta, \eta'\}$ and $\{\alpha, \alpha'\}$ cause an uncertainty in the determination of the bounds $\Delta_b^{(K)}$.

Fig. 8.9 depicts the setup for our verification protocol indicating the losses $\{\eta, \eta'\}$ and beamsplitter ratios $\{\alpha, \alpha'\}$ of the interferometers. Experimental parameters and their uncertainties for $\{\eta, \eta'\}$ and $\{\alpha, \alpha'\}$ are shown in Table 8.1. In our data analysis, we infer the photon statistics of modes $\{1', \cdots, 4'\}$ in $\hat{\rho}_{\text{out}}$ at the outputs of the verification interferometers from the measured photodetection statistics at detectors $\{D_1, \cdots, D_4\}$. Thus, we exclude the losses corresponding to the output paths of the verification interferometers from our analysis. The small imbalances between the terms $\{\alpha, \alpha'\}$ and $\{\eta, \eta'\}$ in Table 8.1 contribute to the small correction of the theoretical bounds $\Delta_b^{(K)}$ from the ideal projectors $|W_i\rangle$ to non-ideal projectors $|\Pi_i\rangle$. To understand the small corrections of $\Delta_b^{(K)}$ from $|W_i\rangle$ to $|\Pi_i\rangle$ for our parameters, we investigate the effect of $\{\eta, \eta'\}$ and $\{\alpha, \alpha'\}$ on the bound $\Delta_b^{(3)}$ for states containing at most tripartite entanglement for a fixed two-photon contamination $y_c = 0.035$, corresponding to the lowest measured y_c in our experiment.

Table 8.1: **Experimental parameters and their uncertainties for beamsplitter ratios $\{\alpha, \alpha'\}$ and transmission efficiencies $\{\eta, \eta'\}$ of the verification interferometers.** The systematic uncertainties $(\delta\kappa)$ of $\{\kappa\}$ are fractionally $(\delta\kappa/\kappa) = 5\%$ for $\kappa \in \{\alpha, \alpha', \eta, \eta'\}$. Note that $\alpha_{12} \simeq \alpha_{34} \simeq \alpha'_{14} \simeq \alpha'_{23}$. The absolute differences in the pairs of transmission efficiencies ($\{\eta_1, \eta_2\}$,$\{\eta_3, \eta_4\}$,$\{\eta'_1, \eta'_4\}$, $\{\eta'_2, \eta'_3\}$) influence the correction to $\Delta_b^{(K)}$.

α_{12}	α_{34}	α'_{23}	α'_{14}	η_1	η_2	η_3	η_4	η'_1	η'_4	η'_2	η'_3
0.5	0.53	0.52	0.53	0.57	0.57	0.52	0.56	0.67	0.66	0.62	0.66

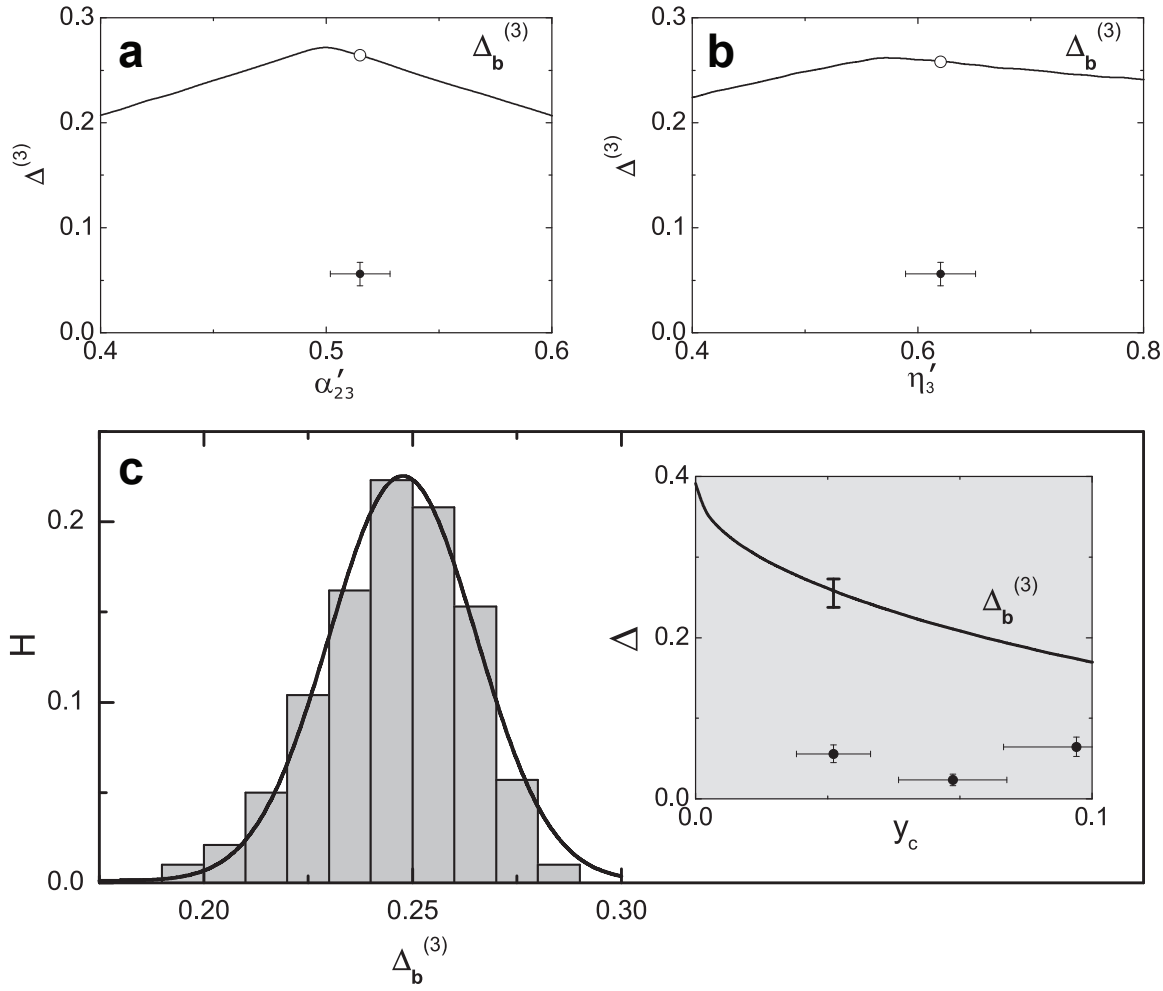

Figure 8.10: **The effect of imbalances and losses to the determination of $\Delta_b^{(3)}$.** Scanning the boundary $\Delta_b^{(3)}$ for states containing at most three-mode entanglement as a function of **a**, the beamsplitter ratio α'_{23} (shown as a black line), and **b**, the transmission efficiency η'_3 (shown as a black line) at $y_c = 0.035$, which corresponds to the lowest two-photon contamination measured in Fig. 8.4. The measured Δ at $y_c = (3.5 \pm 0.9) \times 10^{-2}$ is shown as a filled circle, with a horizontal error indicating the systematic uncertainty in estimating **a**, α'_{23} and **b**, η'_3, respectively. The vertical error is the statistical uncertainty for the measured Δ. **c**, Histogram $H(\Delta_b^{(3)})$ of the three-mode boundary $\Delta_b^{(3)}$ by repeating the calculations from randomly drawn sets of the transmission efficiencies $\{\eta, \eta'\}$ and beamsplitter ratios $\{\alpha, \alpha'\}$ at $y_c = 0.035$. The histogram is fitted to a Gaussian function (shown as a black line) with $(1/e)$ half-width $\delta\Delta_b^{(3)} = 0.018$. The uncertainty $\delta\Delta^{(3)}$ is determined by the joint distribution of $\{\alpha, \alpha'\}$ and $\{\eta, \eta'\}$. Here, we assume independent normal distributions for the individual parameters in $\{\alpha, \alpha'\}$ and $\{\eta, \eta'\}$. (Inset) Confidence level in the violation of the inequality $\Delta \geq \Delta_b^{(3)}$ for the three-mode bound $\Delta_b^{(3)}$. Experimentally measured Δ are shown as filled circles, and the black line indicates the the three-mode bound $\Delta_b^{(3)}$, along with its uncertainty for $y_c = 0.035$. The large suppression of Δ from $\Delta_b^{(3)}$ compared to the uncertainty $\delta\Delta_b^{(3)}$ for the bound affirms the unambiguous detection of genuine four mode entanglement.

Figs. 8.10a and 8.10b illustrate the processes of reductions in the three-mode boundary $\Delta_b^{(3)}$ at $y_c = 0.035$, due to **a**, imbalanced beamsplitter ratio (α'_{23}) and **b**, differential loss (η'_3), while leaving all other parameters in $\{\alpha, \alpha'\}$ and $\{\eta, \eta'\}$ fixed (Table 8.1). In particular, the correction ranges of $\Delta_b^{(3)}$ due to the

individual uncertainties of α'_{23} and η'_3 are small compared to the measured $\sim 20\,\sigma$ (standard deviation) suppression of the sum uncertainty Δ at $y_c = 0.035$ relative to $\Delta_b^{(3)}$ (shown as a filled circle in Fig. 8.10).

Finally, we discuss our analysis of the uncertainty $\delta\Delta_b^{(3)}$ in the bound $\Delta_b^{(3)}$ (Fig. 8.10c) due to the systematic uncertainties of all the parameters in $\{\alpha, \alpha'\}$ and $\{\eta, \eta'\}$. We construct the histogram H of $\Delta_b^{(3)}$ by iterating the calculation of $\Delta_b^{(3)}$ with randomly drawn sets of $\{\alpha, \alpha', \eta, \eta'\}$. Here, the parameters $\{\alpha, \alpha'\}$ and $\{\eta, \eta'\}$ are assumed to follow independent normal distributions, with their means and systematic uncertainties shown in Table 8.1. By fitting the histogram with a Gaussian distribution, we infer an uncertainty $\delta\Delta_b^{(3)} = 0.018$ and the center $\langle\Delta_b^{(3)}\rangle = 0.25$ for the boundary $\Delta_b^{(3)}$. These values should be compared to the measured $\Delta = (5.6 \pm 1.1) \times 10^{-2}$ at $y_c = (3.5 \pm 0.9) \times 10^{-2}$. As depicted in the inset of Fig. 8.10c, our measurement yields $\sim 9\,\sigma$ suppression of the uncertainty bound, reflecting the high confidence level in the violation of the bound $\Delta_b^{(3)}$. Our experiment, therefore, unambiguously verifies the presence of four-mode entanglement with the imbalances $(\{\alpha, \alpha'\}, \{\eta, \eta'\})$ in the verification interferometers.